



# Analysis of Subsonic/Hypersonic Aerodynamics of a High-Speed Aircraft

Giuseppe Pezzella<sup>1</sup> · Antonio Viviani<sup>1</sup>

Received: 16 January 2024 / Revised: 3 March 2024 / Accepted: 8 March 2024  
© The Author(s) under exclusive licence to AIDAA Associazione Italiana di Aeronautica e Astronautica 2024

## Abstract

Unmanned flying-test bed aircraft are fundamental to experimentally prove and validate next-generation high-speed technologies, such as aeroshapes design, thermal protection materials, flight mechanics, and guidance–navigation–control in real flight conditions. During the test, the aircraft will encounter realistic operative conditions to assess the accuracy of new design choices and solutions. In this framework, the paper focuses on the longitudinal aerodynamic analysis of an experimental aircraft, with a spatuled forebody aeroshape, from subsonic up to hypersonic speeds. Computational flowfield analyses are carried out at several angles of attack ranging from 0 to 15° and for Mach numbers from 0.1 to 7. Results are reported in detail and discussed in the paper.

**Keywords** Flying-test bed · Subsonic · Hypersonic · Static stability · Wind tunnel test

## 1 Introduction

In the last decades, attention to high-speed flight has increased dramatically as it represents the next frontier of aerospace applications. This leads to great interests in making reliable, affordable, safe, and maintainable design of high-speed aircraft (HSA). The design of such vehicles is extremely challenging, since several critical flow physics phenomena are involved [1]. Therefore, progress in high-speed technologies strongly rely on the development of flying-test beds (FTBs) [2]. In fact, wind tunnel (WT) test campaigns and flight testing represent the only and ultimate proofs to demonstrate the technical feasibility of next-generation HSA and technologies [3, 4].

In general, the design of HAS relies on two lines, namely, numerical-based design (NBD) and experimental-based design (EBD). In the former, computational fluid dynamics (CFD) represents a tool able to feed the HSA design by means of predictive capabilities, while, in the latter, CFD supports and integrates test campaigns carried out in WT

facilities and in-flight by means of FTBs [5]. In fact, CFD and WT are complementary design tools. During the design phase, aerodynamic and aerothermodynamic characterizations of the vehicle are performed using a hybrid approach that includes WT tests and CFD results. The combined use of WT and CFD is a powerful approach, providing high-quality data as input for performance evaluation, vehicle control, dimensioning, and flight mechanics. Furthermore, HSA designers are well aware that experimental aerodynamic and aerothermodynamic data, fully representative of the flight loading environment, are not always available in ground-based experimental facilities, such as conventional WTs or even high-speed plasma WTs (PWT). Recall that, in general, it is not possible to perform WT tests in which the Mach and Reynolds characteristic numbers of the flight (i.e. the flow similarity parameters) are perfectly duplicated in the same experiment.

In this framework, the paper reports on the longitudinal aerodynamics of the named Vanvitelli-One (V-One) FTB, shown in Fig. 1, see References [6, 7].

The V-One aircraft aims to provide a research platform suitable for a step-by-step increase of the readiness level of several enabling hypersonic technologies by means of both WT and in-flight experimentations. The V-One has a classical lifting-body aeroshape, which embodies all the features of an operational HSA, such as a low aspect ratio double-delta wing, two full movable vertical stabilizers

✉ Antonio Viviani  
antonio.viviani@unicampania.it

Giuseppe Pezzella  
giuseppe.pezzella@unicampania.it

<sup>1</sup> Dipartimento di Ingegneria, Università della Campania “Luigi Vanvitelli”, Via Roma 29, 81031 Aversa, CE, Italy

**Fig. 1** Four views of the concept aeroshape [6, 7]

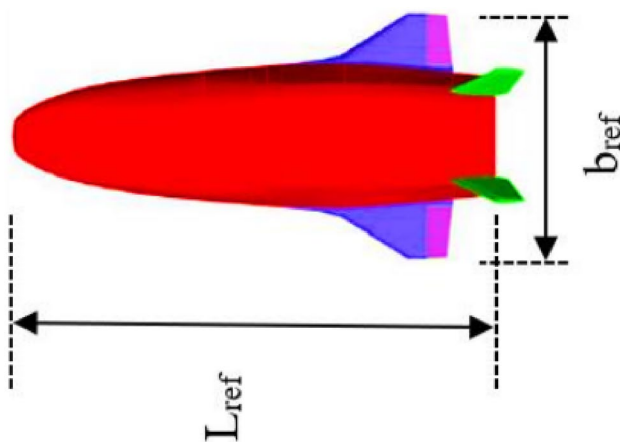
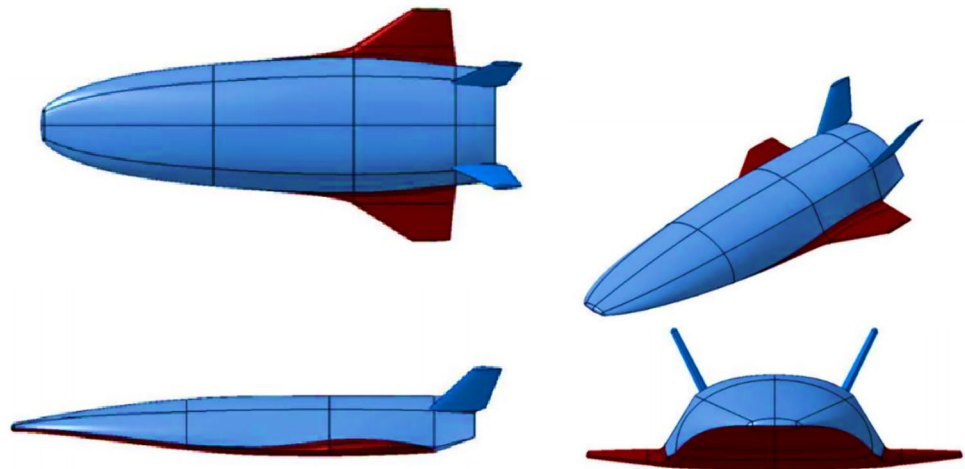


**Fig. 2** Elevons/aileron (in purple) and ruddervators (in green) of the V-One aeroshape

in butterfly configuration, a spatuled fuselage forebody, characterized by a rounded off two-dimensional leading edge, opportunely mated on top of the wing. The wing flaps, which must be actuated as elevons and ailerons, are shown in purple colour in Fig. 2, along with the complete moving fins, the so-called ruddervators, in green colour; the ruddervators are hinged at the 50% of the root chord length [6, 7].

The spatuled-body architecture allows to validate hypersonic aerothermodynamics data and passenger experiments, including thermal shield and hot structures, suitable for the successful development of a full-scale HSA [8, 9]; within a typical mission scenario, in fact, HSA will encounter free-stream flows ranging from hypersonic to low subsonic speeds. Assessment of the V-One longitudinal aerodynamics is undertaken aimed at providing an aerodynamic database (AEDB) to feed flight mechanics performances. The longitudinal aerodynamic analysis is carried out by means of fully three-dimensional CFD simulations at several angles of

attack (AoA), with the goal of providing the relevant aerodynamic coefficients and static stability assessment.

Aircraft aerodynamic force and moment coefficients and static stability highlights in longitudinal flight conditions and for clean configuration are provided and discussed in detail for all the speed flow regimes from subsonic to hypersonic speeds. The values of the force and moment coefficients are provided by means of fully turbulent, three-dimensional numerical simulations carried out at 16 Mach numbers and, for each Mach number, at several angles of attack. Therefore, the aerodynamic results will be presented as function of the AoA for each Mach number, whereas aircraft aerodynamics versus Mach number is provided for selected attitude conditions.

## 2 Aerodynamic Analysis and Numerical Model

Concept longitudinal aerodynamics is addressed in terms of force and moment coefficients, according to ISO-1151 standard, see Fig. 3.

Force and moment coefficients are definite positive as shown in the figure. Lift ( $C_L$ ), drag ( $C_D$ ), and pitching moment ( $C_{M_y}$ ) coefficients are calculated according to the following equations:

$$\begin{cases} C_L = \frac{L}{q_\infty S_{ref}} \\ C_D = \frac{D}{q_\infty S_{ref}} \\ C_{M_y} = \frac{M_y}{q_\infty L_{ref} S_{ref}} \end{cases} \quad (1)$$

The moment coefficient refers to the aircraft moment reference centre (MRC); the reference length,  $L_{ref}$ , coincides with the fuselage length, see Fig. 2, and the vehicle planform area is considered as reference surface,  $S_{ref}$ . In the present case, the reference length,  $L_{ref}$ , is 5 m, while the

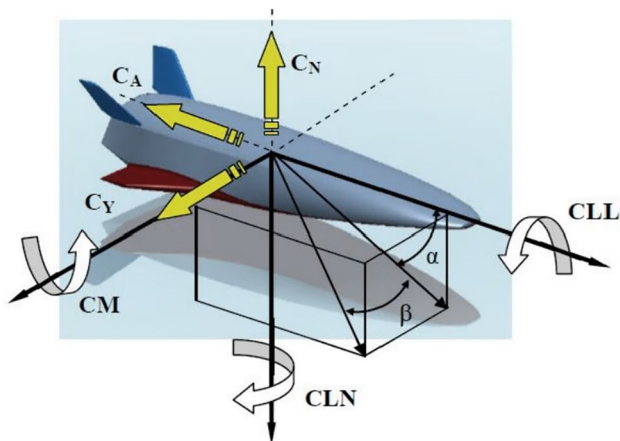


**Fig. 3** Aircraft body reference frame with coefficients sign convention [6, 7]

reference surface,  $S_{ref}$ , is  $4.24 \text{ m}^2$  (half body). CFD analyses, carried out with ANSYS FLUENT<sup>®</sup> tool, address the flowfield past the aircraft for  $\alpha$  ranging from 0 to  $15^\circ$  AoA, for Mach from 0.1 to 7 and for clean configuration only (i.e. no aerodynamic surfaces deflected). Flowfield investigations are obtained by means of steady-state Reynolds averaged Navier–Stokes (RANS) flowfield computations. The pressure-based coupled solver was used for all CFD analyses carried out at free-stream Mach number lower than  $M_\infty=0.3$ ; for Mach higher than this threshold (i.e.  $M_\infty=0.3$ ), the density-based solver with the implicit formulation was considered. In this case, the flux difference splitting (FDS) second-order upwind scheme (least square cell based) was used for the spatial reconstruction of convective terms, while for the diffusive fluxes a cell-centred scheme was applied. An implicit scheme was considered for time integration. For both incompressible and compressible simulations, the k- $\omega$

SST turbulence model was used for Reynolds stress closure due to its ability to model separate flows and regions of flow circulation. Further, the ideal gas model was assumed for air. Recall that, though CFD simulations were carried out at hypersonic flow conditions (up to  $M_\infty=7$ ), the ideal gas assumption was still valid. The reason is that the aero-shape features a very slender configuration and shall fly at rather low AoA (i.e. weak attached shock waves). Anyway, a temperature-dependent formulation was considered for the specific heat at constant pressure,  $c_p$ , to accommodate the rather high flow energy at hypersonic speed [6]. Flow viscosity is given by Sutherland's law. Multi-block structured grids with an overall number of about 10M cells (half body) were considered for the flowfield computations for both low- and high-speed conditions, as shown in Figs. 4 and 5, respectively.

As one can see, two computational domains were generated for the CFD simulations: one for subsonic simulations (see Fig. 4) and the other one for supersonic/hypersonic computations (see Fig. 5). The fluid domain for the subsonic case is a prismatic brick with dimensions of length, width, and depth equal to 50 times the body length (BL) of the aircraft ahead the body and 100 afterwards the aircraft. In fact, due to the rather low free-stream Mach number, a wide mesh domain is needed to avoid reflections of spurious numerical modes arising from the interference of the aircraft with the boundaries of the domain.

On the other hand, for the supersonic case, the computational domain is different with respect to the subsonic one. The supersonic computational domain is shown in Fig. 5, where the mesh on the aircraft wall and symmetry plane is also provided. As bow shocks take place in such a flow regime, a narrowed computational domain can be considered. In fact, due to the hyperbolic nature of the supersonic flowfield equations, it features a paraboloid-like domain.

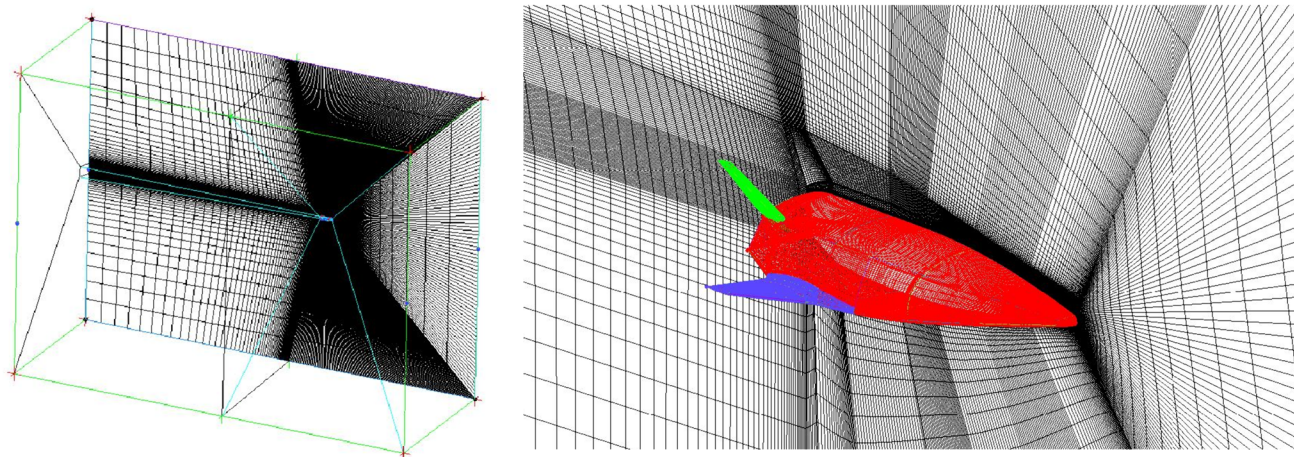


**Fig. 4** Low-speed computational domain and grid

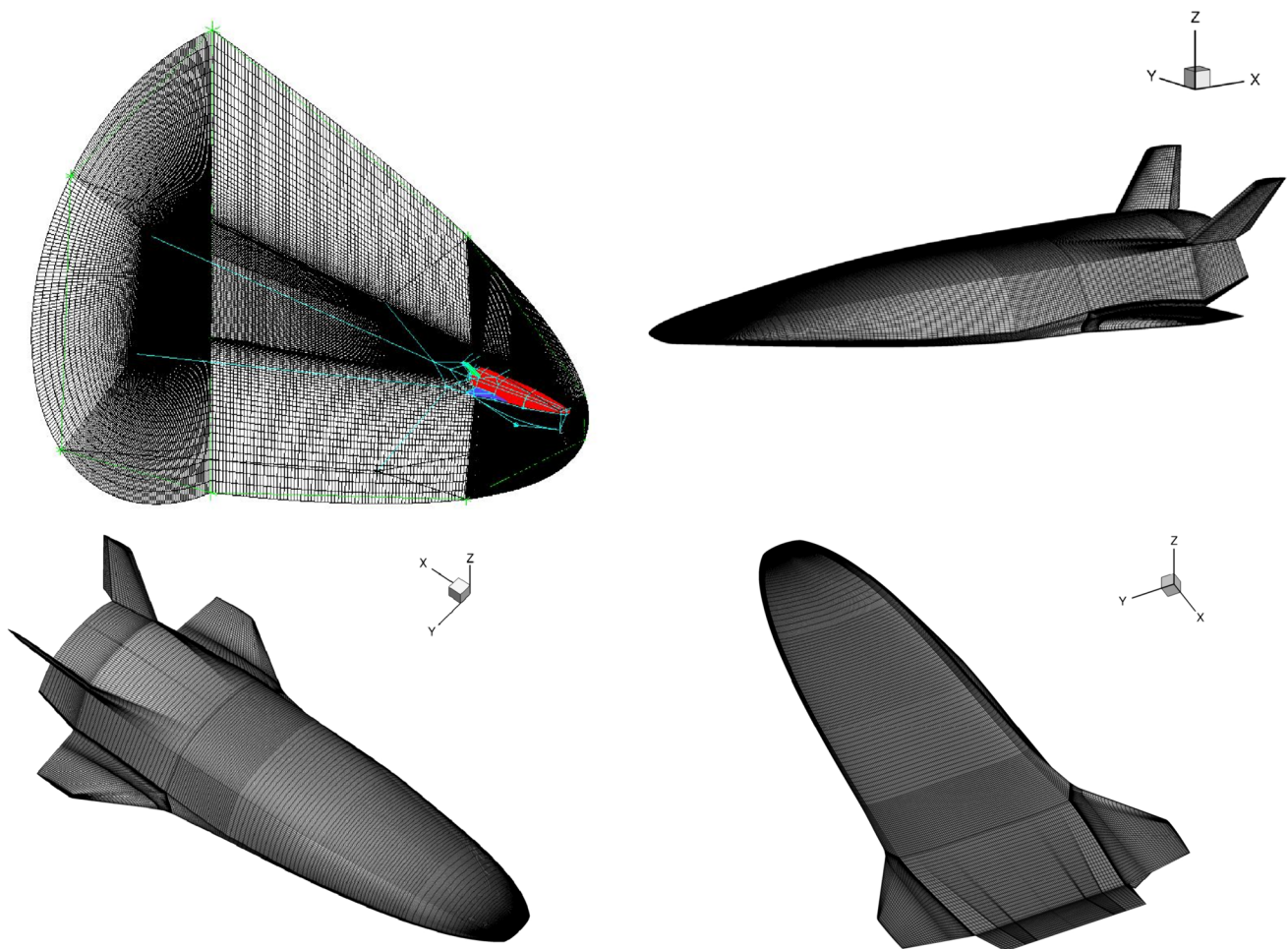


**Fig. 5** High-speed computational domain and grid

Moreover, Figs. 4 and 5 show a denser grid surrounding the vehicle to accurately predict flow behaviour near the body. The grid featured a minimum wall spacing equal to about  $10^{-6}$  m to allow for  $y^+ = O(1)$  and to describe the viscous sublayer. Adiabatic wall boundary condition is assumed at subsonic flow conditions, while the radiative cooled wall ( $\epsilon = 0.8$ ) was assumed in the other cases. As far as solution procedure is concerned, it is worth noting that the solution steering algorithm was considered. It determined the Courant number (CN) during the simulations which affects the solution speed and stability. During solution startup, a CN equal to 1 is considered as changes in the flowfield solution are highly nonlinear. But as computation progresses, solution steering automatically changes some solver parameters and progressively increases the CN to ensure a steady-state-converged solution. Solution steering allows the solver to not exceed the assigned maximum CN and to use a CN less than the initial value if the solution diverges. In addition, full multi-grid initialization is also adopted which computes a quick, simplified solution based on several coarse sub-grids.

This helps to get a stable and better starting field for the main calculation. Under-relaxation factors for the uncoupled parameters are kept at the default values.

Finally, at each CFD simulation, the overall mass, momentum, energy, and scalar balances are verified to address the convergence of the solution. Residuals are verified to have a decrease at least of three orders of magnitude, while the scaled energy residual should decrease to  $10^{-6}$ . Moreover, the numerical computation of each CFD case is stopped and assumed to converge when all aerodynamic coefficient curves also look flat.

### 3 Discussion and Results

The reliability of V-One aerodynamic performance evaluation relies on the accuracy of the present numerical approach (i.e. grids and numerical settings) considered for flowfield simulations. With this in mind, for the subsonic aerodynamics, several CFD computations were preliminarily carried

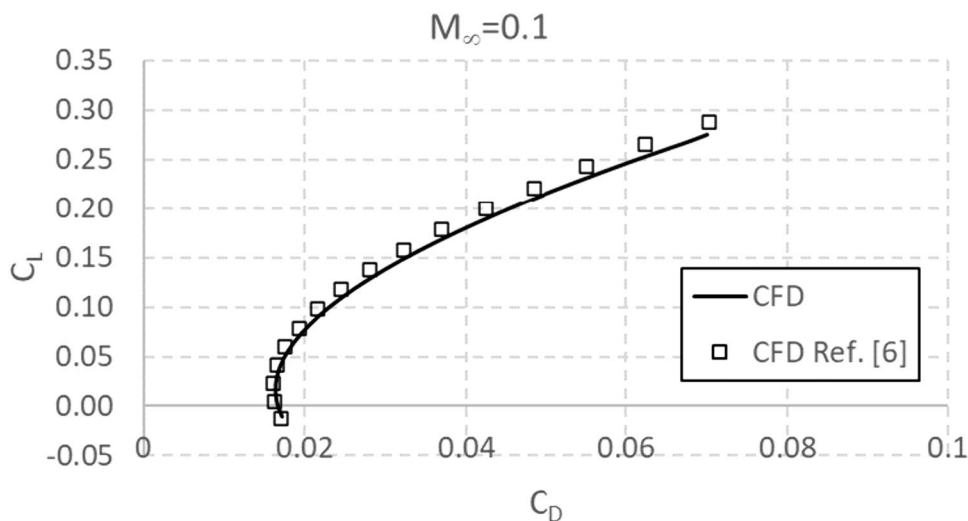
out to numerically rebuild an experimental test campaign performed at the low-speed wind tunnel (WT) of the Department of Engineering of the University of Sydney, within a collaboration research programme [6]. The aim of this research programme was to address both experimental and numerical flowfield investigations of the V-One aeroshape at 30 m/s through a range of AoAs to assess the aerodynamic force and moment coefficients, close to landing conditions. WT tests were completed in the 7×5 foot low-speed facility with a model fabricated using an assembly of three-dimensional printed pieces. The model mounted in the WT test chamber can be seen in Fig. 6. See Refs. [6, 7] for further details.

This WT facility has the capacity to test large models up to 1 or 2 m in length for speeds ranging from 0 to 40 m/s. It is fitted out with state-of-the-art instrumentation and data recording systems for the measurement of air loads,



Fig. 6 V-One model in WT [6, 7]

Fig. 7 Drag polar at  $M_\infty=0.1$ . Comparison between the present CFD and results of Ref. [6]



pressures, and flow fields. The investigations of V-One aeroshape was performed at  $V_\infty=30$  m/s and the test model dimensions provided a Reynolds number of  $1.35 \times 10^6$ . Therefore, this Reynolds number has been set within the CFD simulations to allow a fair comparison between experimental and numerical data.

As first instance, the reliability of low-speed grid was assessed comparing the present CFD results with those independently obtained by researchers in Sydney, with a different grid and a different numerical setting, at  $M_\infty=0.1$  within their activities of numerical rebuilding of WT tests. The comparison of present numerical results with the ones of Sydney is provided in Fig. 7.

In this figure, data are summarized in terms of V-One drag polar at  $M_\infty=0.1$ . As one can see, present numerical results and those of Bykerk et al. compare rather well with each other, thus confirming the reliability of the low-speed computational grid [6].

For what concerns the reliability of the numerical settings, Fig. 8 shows a comparison of the present CFD results for lift, drag, pitching moment coefficients and aerodynamic efficiency with WT data provided in Bykerk et al. [6]. Both experimental and numerical data refer to the same similarity parameters, namely,  $M_\infty=0.09$  and  $Re_\infty=1.35 \times 10^6$ . The moment reference centre (MRC) considered for the pitching moment is at 45% of the body length ( $L_{ref}$ ). As shown, the reliability of the present numerical approach for low-speed flow conditions can be also confirmed by the fact that a fairly good comparison between numerical and experimental data was found [6].

Result comparisons of Fig. 8 allow also inferring low-speed aerodynamics of the V-One aeroshape. For instance, lift coefficient ( $C_L$ ) features a linear curve slope up to about  $\alpha=10^\circ$ , while, at higher attitude, results point out that the  $C_L$  curve deviates from the linear trend. This behaviour is due to the well-known vortex lift phenomenon (VLP). The vehicle

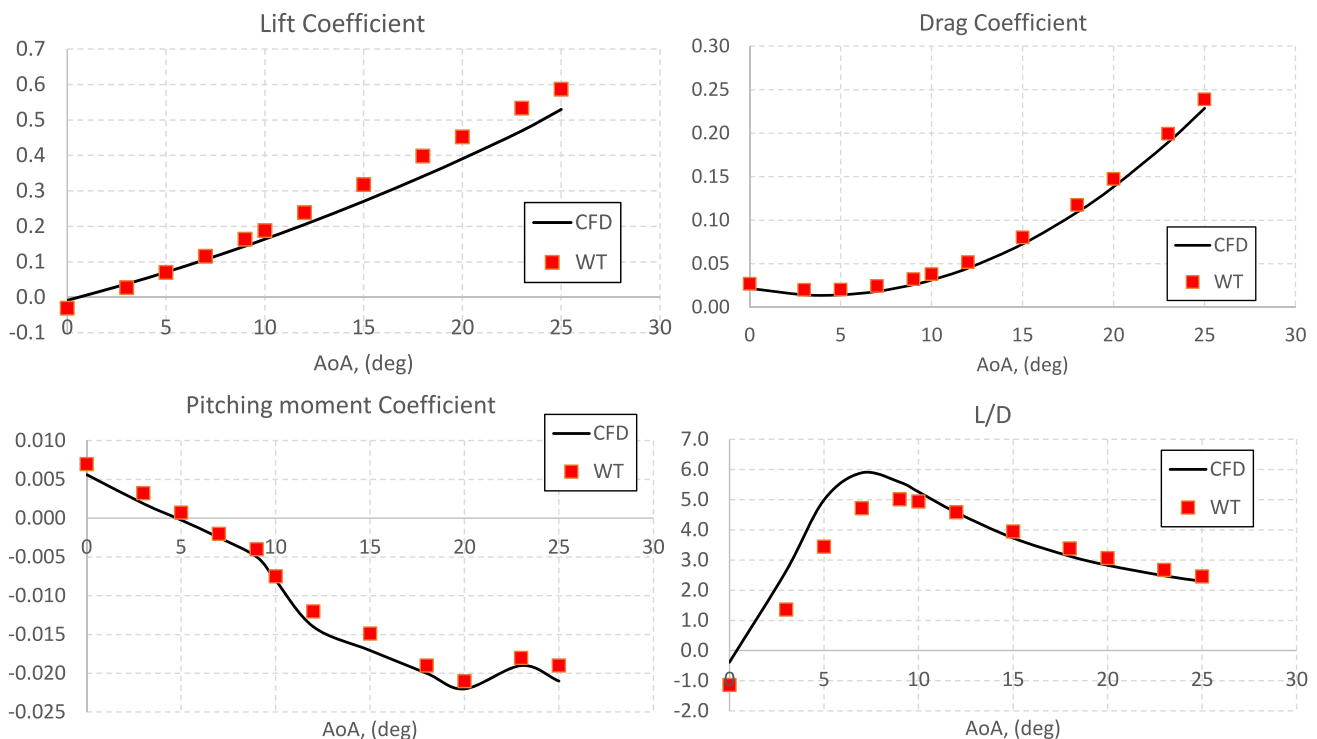


**Fig. 8** Lift, drag, pitching moment (MRC at 0.45%  $L_{ref}$ ) coefficients, and aerodynamic efficiency from 0° to 25°. Comparison between numerical and experimental data obtained for  $M_\infty = 0.09$  and  $Re_\infty = 1.35 \times 10^6$  [6]

aeroshape, in fact, features a double-delta wing planform and a streamlined flat-bottomed and spatuled forebody; see Fig. 1. Thus, flow separation that takes place at the aircraft forebody and wing leading edges when the vehicle is at  $\alpha > 10^\circ$  determines a system of flow vortices which, proceeding along with the aeroshape leeside, determines enhanced local low-pressure conditions. This leads to a nonlinear lift increase despite the low-speed flow regime.

As a further consequence of the VLP, no clear stall condition was identified from the CFD or the WT data up to 25° AoA. A gentle moderate stall is expected at higher attitude close to about 30–35° AoA, according to the typical behaviour of double-delta wings which work with VLP [10, 11]. Flow vortices that take place past the V-One for  $\alpha = 20^\circ$  and  $M_\infty = 0.1$  are shown in Fig. 9.

The pitching moment coefficient versus  $\alpha$  also features a nonlinear trend, according to the  $C_L$  for the same reasons. Both CFD and WT data at  $M_\infty = 0.1$  pointed out that the V-One aeroshape shows a natural trim point at about  $\alpha = 5^\circ$ . Further, the negative slope of the pitching moment curve (i.e.  $C_{M_y} < 0$ ) highlights that this aeroshape is statically stable for longitudinal flight conditions while considering the MRC at 45%  $L_{ref}$ .

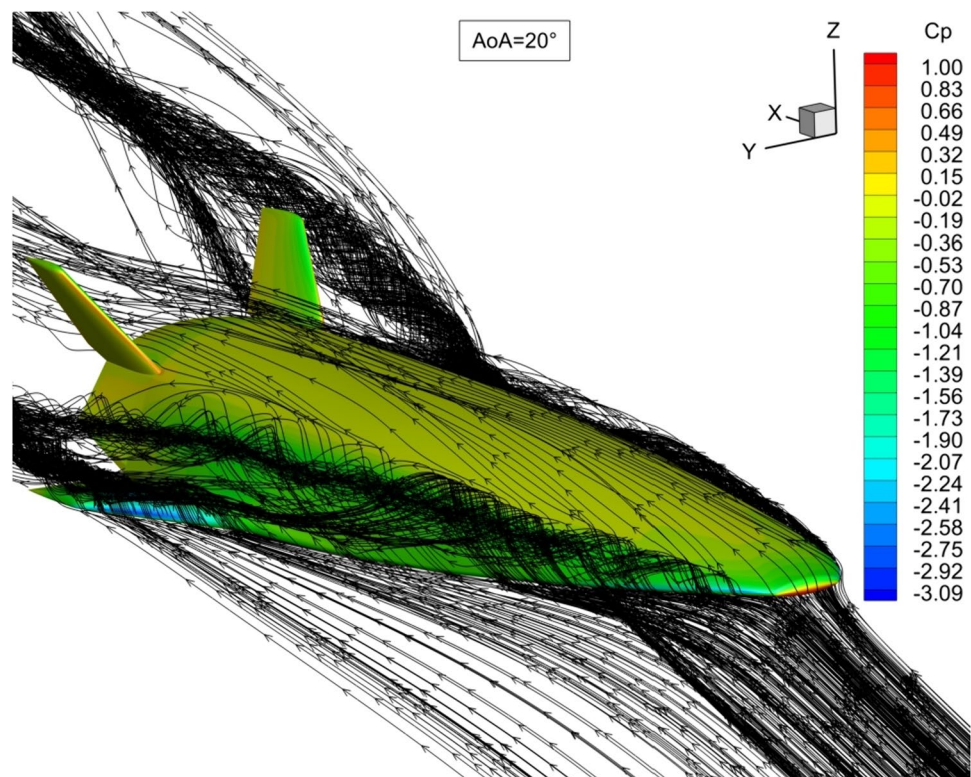
The drag coefficient follows a nonlinear trend, as expected, although the VLP does not appear to

significantly affect this nonlinearity. The maximum lift-to-drag (L/D) ratio is found at about 8° AoA, with an  $(L/D)_{max}$  of approximately 6 and 5 for CFD and WT data, respectively.

As far as high-speed conditions are concerned, it is worth noting that neither CFD data nor WT experimental data are available for the V-One at such flow regime. Therefore, an analysis like that provided in Figs. 7 and 8 is not possible in this case. However, the reliability of numerical investigations at high-speed conditions (i.e. supersonic and hypersonic) can be inferred considering the portfolio of numerical investigation capabilities of the authors, proven and summarized in Refs. [5, 8–10]. Flowfield numerical computations considered 16 Mach numbers, namely,  $M_\infty = 0.1, 0.5, 0.8, 0.9, 0.95, 1.00, 1.05, 1.10, 1.20, 1.30, 1.40, 1.5, 2.0, 3.0, 4.0,$  and 7.0, and 4 angles of attack, namely  $\alpha = 0^\circ, 3^\circ, 5^\circ,$  and  $15^\circ$ . The Reynolds numbers ranged from  $1.38 \times 10^6$  to  $33.3 \times 10^6$ . Therefore, 64 fully three-dimensional and turbulent flowfield simulations were carried out to assess the V-One aerodynamics in the present research effort. For what concerns flowfield results, pressure coefficient ( $c_p$ ) distributions over aircraft aeroshape are provided in Fig. 10 for  $\alpha = 0^\circ$  and different Mach numbers.

For the sake of simplicity, only few  $M_\infty$  are considered in the figure, namely  $M_\infty = 0.1, 0.9, 1.20, 2.0, 4.0,$  and 7.0. Figure 10 provides distributions of  $c_p$  on the aeroshape leeside,

**Fig. 9** Flow vortices of VLP for  $\alpha = 20^\circ$  and  $M_\infty = 0.1$



thus allowing addressing the pressure changes which locally take place while the aircraft accelerates from subsonic to hypersonic speed at  $\alpha = 0^\circ$ . Therefore, it is worth focusing attention on the transonic shock wave, which forms on the wing leeside during the acceleration, and its displacement towards the wing trailing edge as  $M_\infty$  increases. For instance, the remarkable pressure drop visible at  $M_\infty = 0.9$  suggests the presence of a classical supersonic bubble, followed by a transonic shock responsible for the recompression of the flow at the trailing edge of the wing. As the Mach number further increases, the transonic shock moves afterwards, as shown for  $M_\infty = 1.2$ .

The supersonic bubble that takes place on the wing leeside at  $M_\infty = 0.9$  and  $\alpha = 0^\circ$  is clearly visible in Fig. 11 (left side) by considering the wing cross-plane at  $y = 1.17$  m.

In the same figure, the classical fish tail-like shock can be clearly seen for  $M_\infty = 1.2$ , thus confirming the above conclusions about pressure distribution in Fig. 10. The wing bow shock can be also seen in Fig. 11 on the right side. Recall that this flow behaviour has considerable effects on the stability and controllability of the vehicle, as expected when an aircraft goes from low speed to high speed and vice versa, crossing the transonic regime. Indeed, the centre of pressure of the aeroshape is expected to significantly shift afterwards and back.

Finally, as far as hypersonic flow contours are concerned, the Mach number field at  $M_\infty = 7.0$  and  $\alpha = 0^\circ$  is shown in Fig. 12 considering the aircraft symmetry plane (left side)

and the wing plane (right side). The complex and narrow shock layer which forms at hypersonic speed is clearly recognizable. This determines rather high aerothermal load on the aeroshape forebody and wing–tail leading edges. In particular, on the outer wing leading edge a shock–shock phenomenon is also expected, with consequent local pressure and heat flux overshoots.

The Mach contours which take place in the wing cross-plane at  $y = 1.17$  m for  $M_\infty = 4.0$  and  $7.0$  are provided in Fig. 13. As shown, a rather strong shock wave detaches from the leading edge due to the hypervelocity flow conditions, while trailing edge recompression shocks form at wing trailing edges, thus limiting the viscous wake flow behind the body.

The trace of aircraft bow shock on the wing cross-plane is also clearly evident in Fig. 13. Aerodynamic results in terms of lift, drag, and pitching moment coefficients at different  $M_\infty$  are summarized from Figs. 14, 15, 16, and 17. Figures 14 and 15 provide  $C_L$ ,  $C_D$ , and  $C_{M_y}$  versus  $M_\infty$  for  $\alpha = 0^\circ, 3^\circ, 5^\circ$ , and  $15^\circ$ , while Figs. 16 and 17 show V-One drag polars and pitching moment coefficients (MRC at  $0.45\% L_{ref}$ ) for low speeds (i.e.  $M_\infty = 0.5, 0.9$ , and  $1.0$ ) and high speeds (i.e.  $M_\infty = 1.1, 1.5, 3.0$ , and  $7.0$ ).

As shown in Fig. 14, lift and drag coefficients rise in the transonic region and, as expected, grow as  $\alpha$  increases. Indeed, the aerodynamic characteristics of aircraft are subjected to the well-known compressibility crisis, which is clearly evident from the rapid increase of coefficients

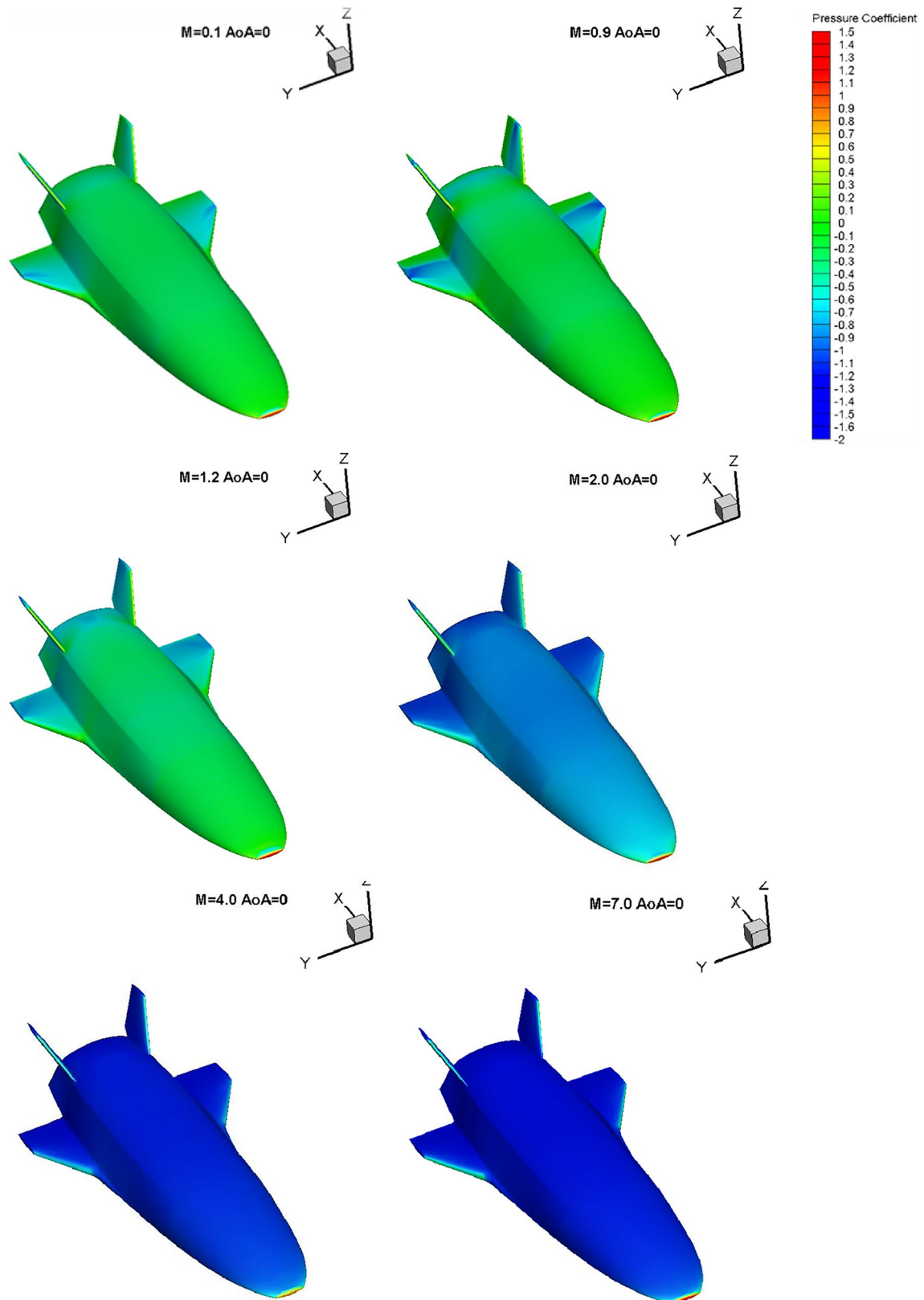


Fig. 10 Pressure coefficient distributions for  $M_\infty=0.1, 0.9, 1.2, 2.0, 4.0,$  and  $7.0$  at  $\alpha=0^\circ$



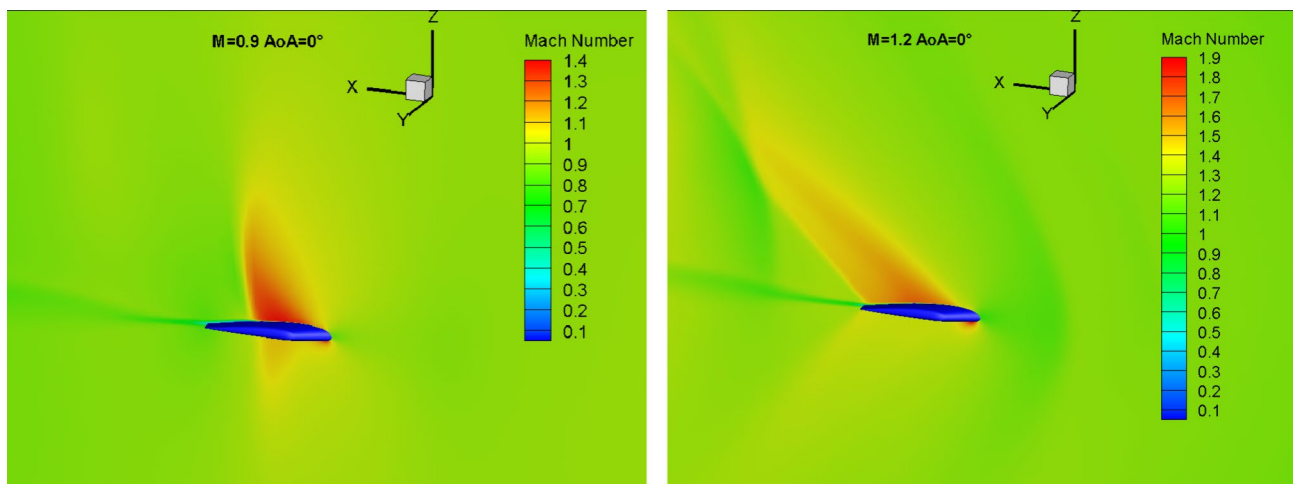


Fig. 11 Mach number contour fields for  $M_\infty = 0.9$  and  $1.2$  at  $\alpha = 0^\circ$  in the wing cross-plane at  $y = 1.17$  m

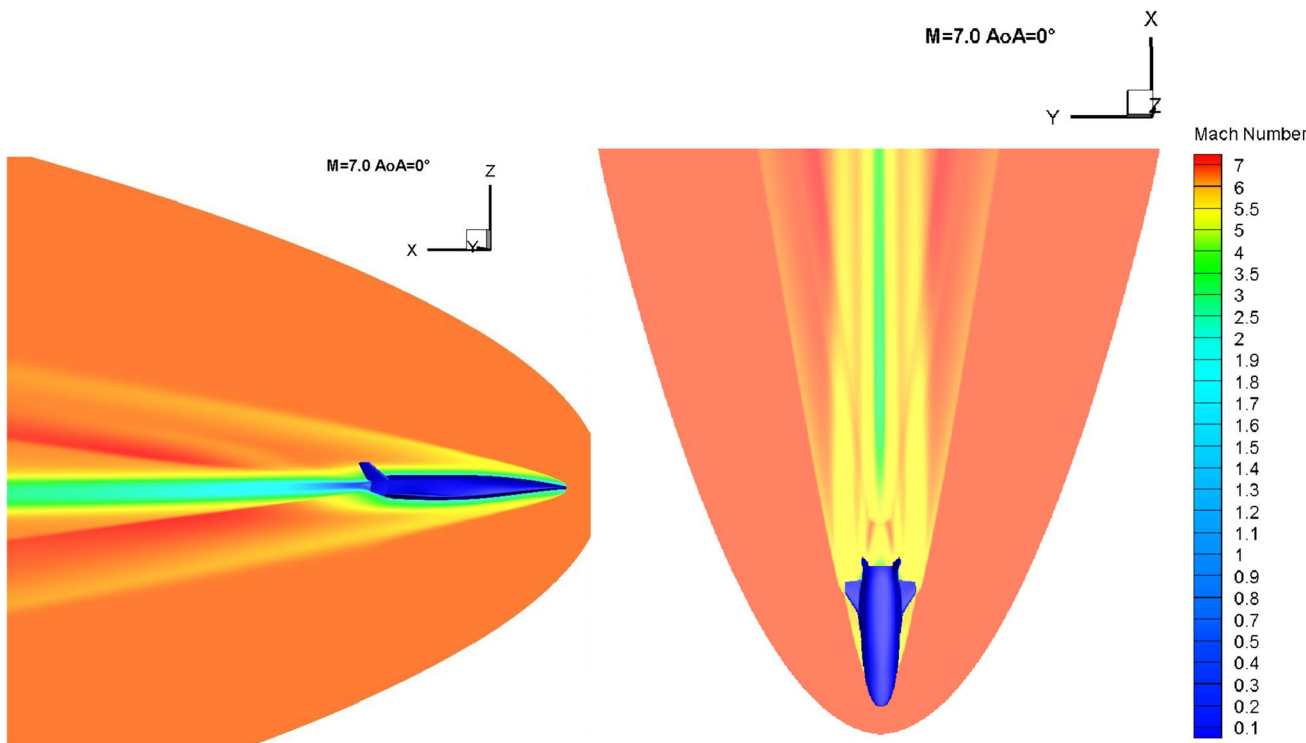


Fig. 12 Mach number contour fields for  $M_\infty = 7.0$  at  $\alpha = 0^\circ$  in the aircraft symmetry plane and wing plane

around  $M_\infty = 1$ . As the aircraft approaches the speed of sound, in fact, the flowfield past the vehicle is characterized by the presence of shock waves. As a result, aerodynamic forces and moments change from those experienced at incompressible flow conditions. Aircraft drag sharply rises, starting from the drag divergence Mach number, due to the wave drag. For the reasons mentioned above, the drag coefficient of the aircraft close to sonic speed is greater than that in the supersonic range due to

the erratic shock formation and general flow instabilities, typical of the flowfield around  $M_\infty = 1$ . However, once supersonic flow is established, the flow stabilizes, and the drag coefficient is reduced. When the Mach number further increases up to hypersonic speeds, aerodynamic coefficients decrease and reach a limit value, according to the Mach number independence principle. Drag polars of Fig. 16 change according to Fig. 14. At subsonic flow conditions, vehicle drag increases essentially due to lift

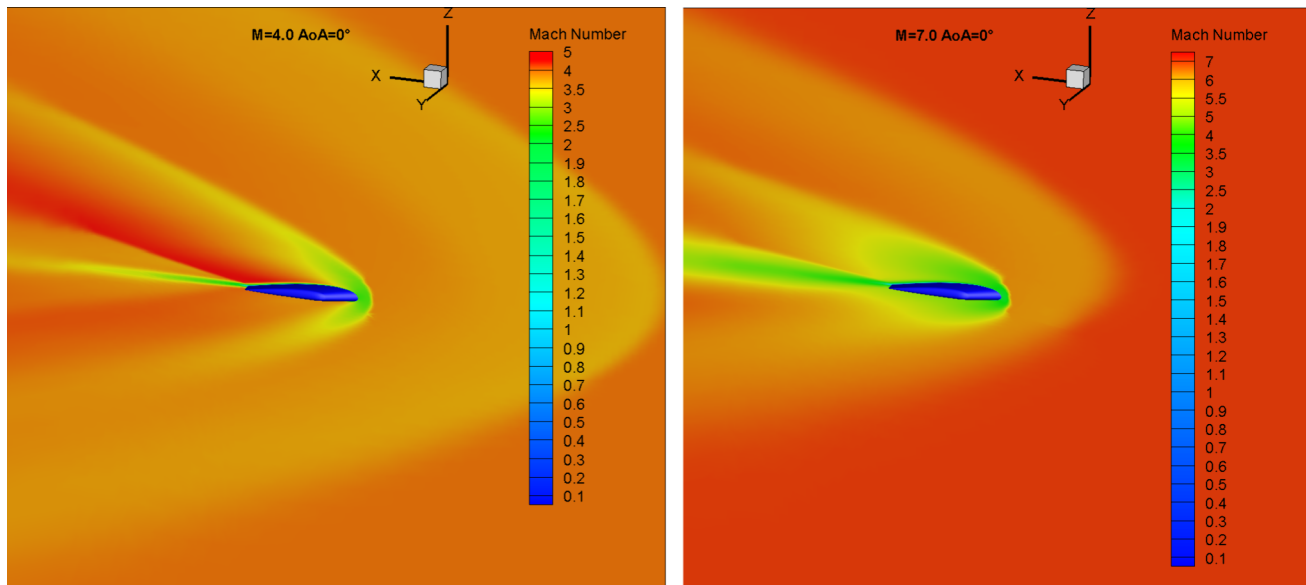


Fig. 13 Mach number contour fields for  $M_\infty = 4.0$  and  $7.0$  at  $\alpha = 0^\circ$  in the wing cross-plane at  $y = 1.17$  m

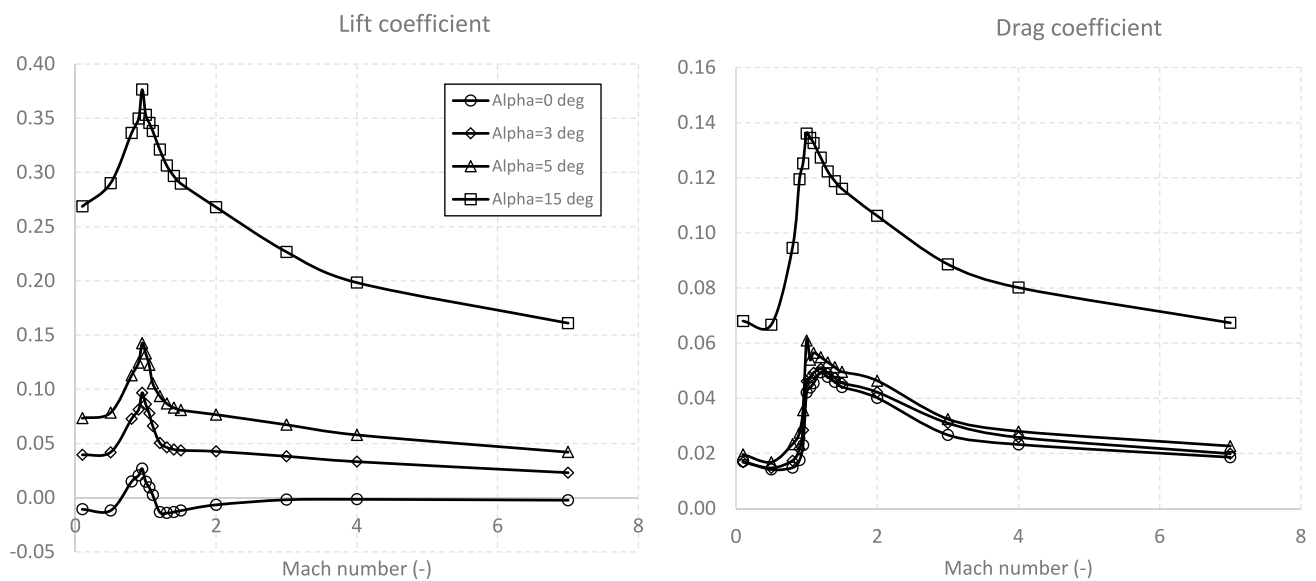


Fig. 14 Lift and drag coefficients versus Mach at  $\alpha = 0^\circ, 3^\circ, 5^\circ,$  and  $15^\circ$

(i.e. induced drag,  $C_{Di}$ ). However, as soon as the aircraft proceeds at Mach number larger than the lower critical Mach number, vehicle drag is essentially due to wave drag as  $C_{Di}$  tends to vanish.

Finally, the displacement of the centre of pressure location ( $x_{cp}/L_{ref}$ ) of the aircraft versus Mach is provided in Fig. 18 for  $\alpha = 3^\circ, 5^\circ,$  and  $15^\circ$ .

As stated above, results summarized in Fig. 18 suggest that strong longitudinal instabilities can be expected for the V-One aeroshape, while the aircraft crosses the transonic speed range.

## 4 Conclusions

Flying-test bed vehicles are an efficient way to experimentally validate next-generation high-speed technologies in real flight conditions. In this framework, the paper focused attention on the appraisal of the longitudinal aerodynamic performance of a streamlined flying-test bed aircraft with a spatulated forebody aeroshape, named V-One. Several computational flowfield analyses were carried out at angles of

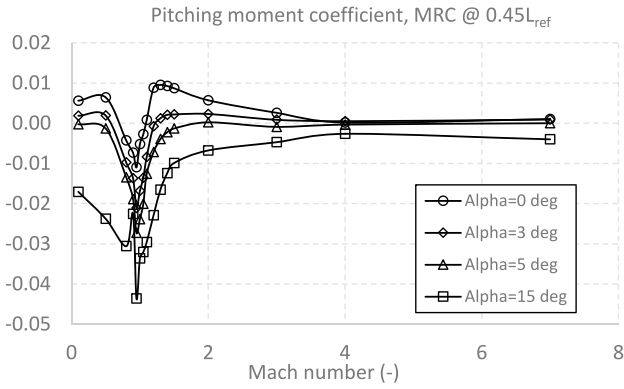


Fig. 15 Pitching moment coefficients versus Mach at  $\alpha=0^\circ, 3^\circ, 5^\circ,$  and  $15^\circ$

attack ranging from 0 to  $15^\circ$  and for Mach numbers from 0.1 to 7.

Numerical results pointed out that low-speed aerodynamics of the V-One aerospace is characterized by the well-known vortex lift phenomenon. The vehicle aerospace, in fact, features a double-delta wing planform and a streamlined flat-bottomed and spatulated forebody. This means that the lift coefficient features a linear curve slope only up to about  $\alpha = 10^\circ$ , while, at higher attitude, the lift curve deviates from the linear trend. The same behaviour was observed for the pitching moment coefficient. The drag coefficient features the classical nonlinear variation because of the induced drag.

As far as hypersonic flow conditions are concerned, lift, drag, and pitching moment coefficients are characterized by a nonlinear trend already at low attitude conditions, according to the characteristic of hypervelocity flows.

Furthermore, the V-One aerospace is statically stable for longitudinal flight conditions if the moment reference point

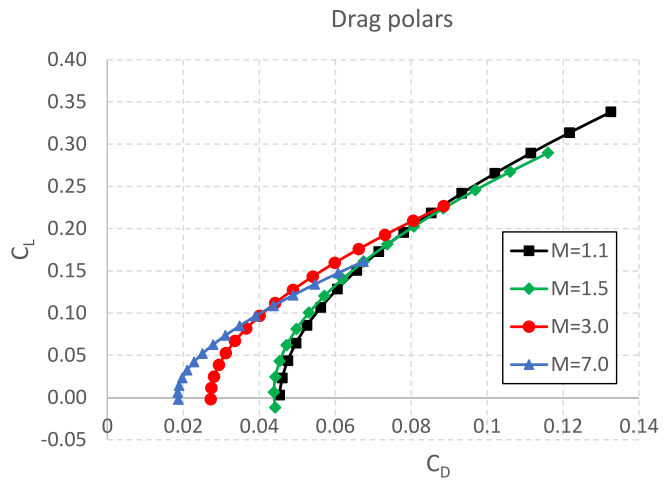
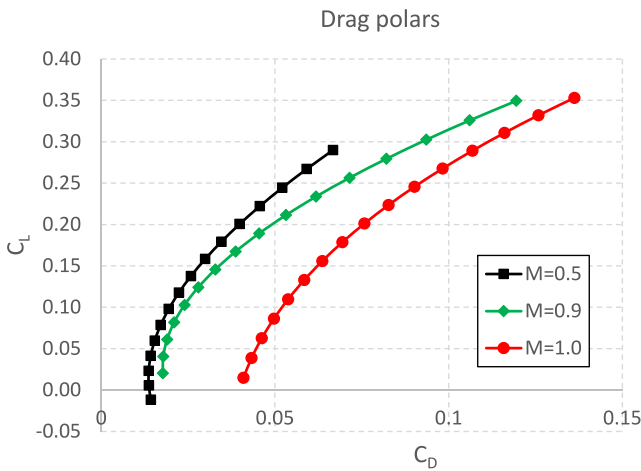


Fig. 16 Aircraft drag polars at  $M_\infty=0.5, 0.9, 1.0, 1.1, 1.5, 3.0,$  and  $7.0$

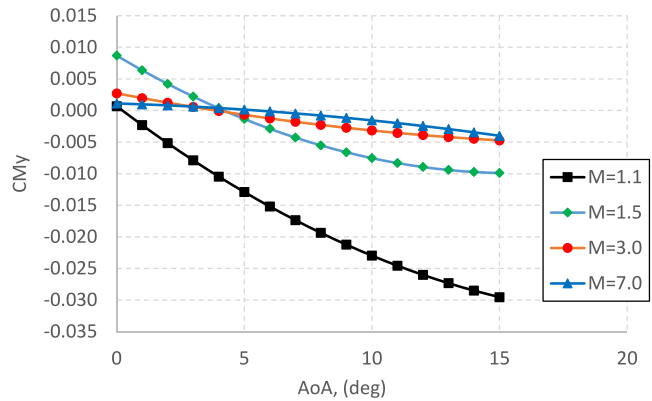
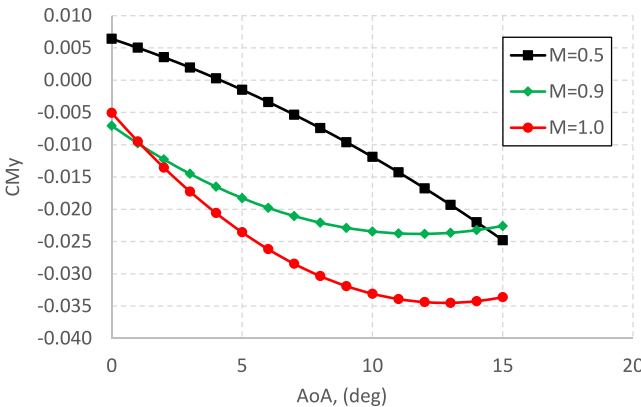
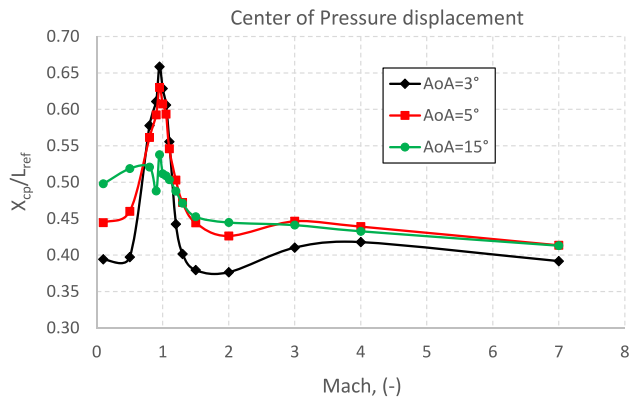


Fig. 17 Aircraft pitching moment coefficients (MRC at  $0.45L_{ref}$ ) at  $M_\infty=0.5, 0.9, 1.0, 1.1, 1.5, 3.0,$  and  $7.0$



**Fig. 18** Centre of pressure location ( $x_{cp}/L_{ref}$ ) versus  $M_\infty$  at  $\alpha=3^\circ$ ,  $5^\circ$ , and  $15^\circ$

is assumed at the 45% of the fuselage length starting from the nose.

**Author Contributions** A.V. wrote the main manuscript text and G.P. prepared all figures. All authors reviewed the manuscript.

**Data availability** No datasets were generated or analysed during the current study.

## Declarations

**Conflict of interest** The authors declare no competing interests.

## References

- Bertin, J.J., Cummings, R.M.: Fifty years of hypersonics: where we've been, where we're going. *Prog. Aerosp. Sci.* **39**(6–7), 511–536 (2003)
- McClinton, C. R., Rausch, V. L., Nguyen, L. T., Sitz, J. R., “Preliminary X-43 flight test results”, *Acta Astronautica*, Volume 57, Issues 2–8, 2005, Pages 266–276, ISSN 0094–5765, <https://doi.org/10.1016/j.actaastro.2005.03.060>.
- Jeyaratnam, J., Bykerk, T., Verstraete, D.: Low speed stability analysis of a hypersonic vehicle design using CFD and wind tunnel testing. In: 21st AIAA International Space Planes and Hypersonics Technologies Conference, Hypersonics **2017**, 10 (2017). <https://doi.org/10.2514/6.2017-2223>.
- Bykerk, T., Verstraete, D., Steelant, J.: Low speed lateral-directional dynamic stability analysis of a hypersonic waverider using unsteady Reynolds averaged Navier Stokes forced oscillation simulations. *Aerosp. Sci. Technol.* **106**, 106228 (2020). <https://doi.org/10.1016/j.ast.2020.106228>
- Viviani, A., Aprovitola, A., Pezzella, G., Rainone C.: CFD design capabilities for next generation high-speed aircraft. *Acta Astronaut.* **178**, 143–158 (2021) (ISSN: 0094–5765). <https://doi.org/10.1016/j.actaastro.2020.09.006>. <https://www.sciencedirect.com/science/article/pii/S0094576520305439>
- Bykerk, T., Pezzella, G., Verstraete, D., Viviani, A.: High and low speed analysis of a re-usable unmanned re-entry vehicle. *HISST. International Conference on High-Speed Vehicle Science and Technology. Moscow. Russia. hisst-2018\_1620897* (2018)
- Bykerk, T., Pezzella, G., Verstraete, D., Viviani, A.: Lateral-directional aerodynamics of a re-usable re-entry vehicle. In: 8th European Conference for Aeronautics and Space Sciences (Eucass-2019), Madrid (2019)
- Scigliano, R., Pezzella, G., Di Benedetto, S., Marini, M., Steelant, J.: Hexafly-int experimental flight test vehicle (EFTV) aerothermal design. In: *Proceedings of the ASME 2017 International Mechanical Engineering Congress and Exposition IMECE 2017. November 3–9, 2017, Tampa, Florida, USA. ASME 2017 International Mechanical Engineering Congress and Exposition Volume 1: Advances in Aerospace Technology Tampa, Florida, USA, November 3–9, 2017. Conference Sponsors: ASME. ISBN: 978-0-7918-5834-9. Paper No. IMECE2017–70392, pp. V001T03A022; 14 pages.* <https://doi.org/10.1115/IMECE2017-70392>
- Schettino, A., Pezzella, G., Marini, M., Di Benedetto, S., Villace, V.F., Steelant, J., Choudhury, R., Gubanov, A., Voevodenko, N.: Aerodynamic database of the HEXAFly-INT hypersonic glider. *CEAS Space J* **12**(2), 295–311 (2020). <https://doi.org/10.1007/s12567-020-00299-4>
- Viviani, A., Aprovitola, A., Iuspa, L., Pezzella, G.: Aeroshape design of reusable re-entry vehicles by multidisciplinary optimization and computational fluid dynamics. *Aerosp. Sci. Technol.* (2020). <https://doi.org/10.1016/j.ast.2020.106029>. (ISSN: 1270-9638)
- Viviani, A., Aprovitola, A., Iuspa, L., Pezzella, G.: Low speed longitudinal aerodynamics of a blended wing-body re-entry vehicle. *Aerosp. Sci. Technol.* (2020). <https://doi.org/10.1016/j.ast.2020.106303>. <https://www.sciencedirect.com/science/article/pii/S1270963820309858>. (ISSN: 1270-9638)

**Publisher's Note** Springer Nature remains neutral with regard to jurisdictional claims in published maps and institutional affiliations.

Springer Nature or its licensor (e.g. a society or other partner) holds exclusive rights to this article under a publishing agreement with the author(s) or other rightsholder(s); author self-archiving of the accepted manuscript version of this article is solely governed by the terms of such publishing agreement and applicable law.